Tracing the young massive high-eccentricity binary system θ¹ Orionis C through periastron passage ★

S. Kraus[1], G. Weigelt[1], Y. Y. Balega[2], J. A. Docobo[3], K.-H. Hofmann[1], T. Preibisch[4], D. Schertl[1], V. S. Tamazian[3], T. Driebe[1], K. Ohnaka[1], R. Petrov[5], M. Schöller[6], and M. Smith[7]

[1] Max-Planck-Institut für Radioastronomie, Auf dem Hügel 69, 53121 Bonn, Germany
[2] Special Astrophysical Observatory, Russian Academy of Sciences, Nizhnij Arkhyz, Zelenchuk region, Karachai-Cherkesia, 357147, Russia
[3] Astronomical Observatory R. M. Aller, University of Santiago de Compostela, Galicia, Spain
[4] Universitäts-Sternwarte München, Scheinerstr. 1, 81679 München, Germany
[5] Laboratoire Universitaire d'Astrophysique de Nice, UMR 6525 Université de Nice/CNRS, Parc Valrose, 06108 Nice Cedex 2, France
[6] European Southern Observatory, Karl-Schwarzschild-Str. 2, 85748 Garching, Germany
[7] Centre for Astrophysics & Planetary Science, University of Kent, Canterbury CT2 7NH, UK

ABSTRACT

Context. The nearby high-mass star binary system θ¹ Ori C is the brightest and most massive of the Trapezium OB stars at the core of the Orion Nebula Cluster, and it represents a perfect laboratory to determine the fundamental parameters of young hot stars and to constrain the distance of the Orion Trapezium Cluster.

Aims. By tracing the orbital motion of the θ¹ Ori C components, we aim to refine the dynamical orbit of this important binary system.

Methods. Between January 2007 and March 2008, we observed θ¹ Ori C with VLTI/AMBER near-infrared (*H*- and *K*-band) long-baseline interferometry, as well as with bispectrum speckle interferometry with the ESO 3.6 m and the BTA 6 m telescopes (*B′*- and *V′*-band). Combining AMBER data taken with three different 3-telescope array configurations, we reconstructed the first VLTI/AMBER closure-phase aperture synthesis image, showing the θ¹ Ori C system with a resolution of ∼ 2 mas. To extract the astrometric data from our spectrally dispersed AMBER data, we employed a new algorithm, which fits the wavelength-differential visibility and closure phase modulations along the *H*- and *K*-band and is insensitive to calibration errors induced, for instance, by changing atmospheric conditions.

Results. Our new astrometric measurements show that the companion has nearly completed one orbital revolution since its discovery in 1997. The derived orbital elements imply a short-period ($P \approx 11.3$ yr) and high-eccentricity orbit ($e \approx 0.6$) with periastron passage around 2002.6. The new orbit is consistent with recently published radial velocity measurements, from which we can also derive the first direct constraints on the mass ratio of the binary components. We employ various methods to derive the system mass ($M_{\mathrm{system}} = 44 \pm 7\ M_{\odot}$) and the dynamical distance ($d = 410 \pm 20$ pc), which is in remarkably good agreement with recently published trigonometric parallax measurements obtained with radio interferometry.

Key words. stars: formation – stars: fundamental parameters – stars: individual: θ¹ Ori C – binaries: close – techniques: interferometric

1. Introduction

The Orion Nebula (M42) is one of the closest ($d \sim 400 - 450$ pc) and most prominent star-forming regions (see O'Dell 2001 for a review). It contains a massive cluster of very young ($\sim 1 \times 10^6$ yr) stars (cf. Herbig & Terndrup 1986; McCaughrean & Stauffer 1994; Hillenbrand 1997), which is known as the Orion Nebula Cluster (ONC). Due to its relatively close distance and its favorable celestial location (which makes it ac-

cessible to observatories on the northern and southern hemispheres), the ONC is probably the best investigated young cluster in the whole sky and has been observed at virtually every wavelength. It is a perfect laboratory for observations of young stellar objects over the full mass range, from very low-mass brown dwarfs to massive O-type stars.

The brightest star in the cluster is the massive O7–O5.5 type [1] star θ¹ Ori C, which is known to be a close visual binary system. After the initial discovery of the companion at a

---

Send offprint requests to: skraus@mpifr-bonn.mpg.de

★ Based on observations made with ESO telescopes at the La Silla Paranal Observatory under programme IDs 078.C-0360(A), 080.C-0541(A,B,C,D), 080.D-0225(B), and 080.C-0388(A).

[1] Simón-Díaz et al. (2006) determined the stellar effective temperature of θ¹ Ori C to be $T_{\mathrm{eff}} = 39\,000 \pm 1\,000$ K with $\log g = 4.1$ dex. In recent stellar atmosphere models (Martins et al. 2005), this corresponds to a spectral type of O5.5–O6, while the same parameters

separation ρ of 0.′′033 (33 mas, corresponding to about 15 AU) with near-infrared (NIR) bispectrum speckle interferometry by Weigelt et al. (1999), Schertl et al. (2003) have presented further observations and reported the first detection of orbital motion. Kraus et al. (2007) presented the first speckle observations at visual wavelengths, the first NIR long-baseline interferometric observations of θ^1 Ori C using the IOTA interferometer, and produced an aperture-synthesis image of the system. They also performed a joint analysis of all existing interferometric measurements that covered a period of more than 9 years and clearly revealed orbital motion. After reaching a maximum value of 42 mas in 1999, the separation of the system steadily decreased to 13 mas in 2005. Detailed modeling of these data yielded a preliminary orbit solution with a high eccentricity ($e \sim 0.91$) and a period of 10.9 yrs. According to this solution, the periastron passage should have occurred around July 2007 with a closest separation of less than 2 AU. Patience et al. (2008) recently presented additional interferometric observations of θ^1 Ori C obtained with NPOI at visual wavelengths. Extending the orbital coverage by about 1.2 yrs, they measured a companion position which deviates ~ 4 mas from the position predicted by the orbital solution of Kraus et al. (2007) and concluded that the orbit has a considerably lower eccentricity ($e \sim 0.16$) and a longer period (~ 26 yrs). This shows a clear need for further interferometric observations that will clarify this apparent discrepancy. A reliable and accurate orbit solution will also provide unique constraints to the basic stellar parameters and, most importantly, will yield the masses of the stars and the distance.

The orbital motion of the companion might also be responsible for the radial velocity variations reported by Stahl et al. (1996, 2008) and others. Due to the incomplete coverage and the significant scatter in the derived velocities, it is not yet possible to derive the orbital elements of the spectroscopic orbit (Stahl et al. 2008).

In spite of its importance and the huge number of studies, the distance to the ONC is, even after decades of investigation, still not well known and an issue of ongoing discussion. The "canonical" value of 450 pc (Herbig & Terndrup 1986; Genzel & Stutzki 1989) that was widely used during the last two decades was recently challenged by some studies finding significantly smaller values. Numerous new distance determinations (e.g. Stassun et al. 2006; Jeffries 2007; Mayne & Naylor 2008), also including the first direct trigonometric parallax measurements on radio sources in the ONC by Hirota et al. (2007, 437 ± 19 pc), Sandstrom et al. (2007, 389^{+24}_{-21} pc), and Menten et al. (2007, 414 ± 7 pc), yielded distances mainly in the range between 390 pc and 440 pc. The $\sim 13\%$ difference in these distance estimates, which to some extent might also include an intrinsic distance spread of the studied stars, leads to an $\sim 30\%$ uncertainty in the derived stellar luminosities and correspondingly affects any age and mass estimates for the stars. This is a serious limitation to the usefulness of the exceptionally well-studied young stellar population; e.g., for the calibration of pre-main-sequence evolutionary models or in the in-

correspond to a later spectral type of O7.5–O8 using earlier models (e.g. Vacca et al. 1996).

Table 2. AMBER calibrator stars and their characteristics, including uniform disk (UD) diameters.

Star	V	H	K	Spectral Type	Adopted UD diameter [mas]
HD 33833	5.9	3.9	3.8	G7III	0.83 ± 0.06^a
HD 37128	1.7	2.4	2.3	B0I	0.86 ± 0.16^b
HD 41547	5.9	5.1	5.0	F4V	0.41 ± 0.03^a
HD 43023	5.8	3.7	3.5	G8III	0.98 ± 0.07^a
HD 50281	6.6	4.3	4.1	K3V	0.77 ± 0.10^c

Notes – [a] UD diameter computed with ASPRO (http://www.jmmc.fr/aspro_page.htm).
[b] UD diameter taken from Mozurkewich et al. (1991).
[c] UD diameter taken from getCal tool (http://mscweb.ipac.caltech.edu/gcWeb/).

vestigation of the spatial relationship between the young stellar groups in the wider region of the Orion association. Therefore, trigonometric parallax measurements of stars in the core of the Trapezium OB star cluster (e.g. on GMR 12=θ^1 Ori A2, for which Menten et al. 2007 measured 418 ± 9 pc) are highly desirable. An alternative way to obtain such distance estimates is through astrometric measurements on close binary systems such as θ^1 Ori C, yielding the dynamical parallax of the system.

2. Observations and data reduction

2.1. Bispectrum speckle interferometry

Bispectrum speckle interferometry is a powerful technique to overcome atmospheric perturbations and to reach the diffraction-limited resolution of ground-based telescopes at visual wavelengths. After monitoring the orbital evolution of the system between 1997 and 2004 at wavelengths between 2.1 μm and 545 nm ($\rho = 43 \ldots 24$ mas; Weigelt et al. 1999; Schertl et al. 2003; Kraus et al. 2007) using the Russian *Big Telescope Alt-azimuthal* (BTA) 6.0 m telescope, θ^1 Ori C became unresolvable with 6 m-class telescopes in 2006. In November 2007 ($\rho = 20$ mas) and January 2008, the system could again be resolved with the BTA 6 m telescope using a V' medium-band filters ($\lambda_c = 550$ nm, $\Delta\lambda = 20$ nm). For these observations, a 1280×1024 pixel CCD with a multi-alkali S25 intensifier photocathode was used.

In January 2008, additional speckle measurements using V' ($\lambda_c = 550$ nm, $\Delta\lambda = 30$ nm) and B' ($\lambda_c = 440$ nm, $\Delta\lambda = 16$ nm) medium-band filter were obtained with the ESO 3.6 m telescope. The speckle observations were carried out in the course of ESO open-time programme 080.C-0388(A) using our visitor speckle camera, which employs a Marconi/EEV electron-multiplying CCD. For the speckle observations, we recorded interferograms of θ^1 Ori C and of nearby unresolved stars in order to compensate for the atmospheric speckle transfer function. The calibrator stars, the number of recorded interferograms and the detector integration times (DITs) are listed in Table 1. The modulus of the Fourier transform of the object (visibility) was obtained with the speckle interferometry

Table 1. Observation log for our new bispectrum speckle and long-baseline interferometric observations.

Instrument	Date [UT]	UT	Telescope Triplet	Spectral Mode	DIT	No. Interferograms Target/Calibrator	Calibrator(s)
BTA 6 m/Speckle	2007 Nov 25			550 nm/20 nm	20 ms	1940/1940	θ^1 Ori D
ESO 3.6 m/Speckle	2008 Jan 10			440 nm/16 nm	10 ms	18000/10000	36 Ori
ESO 3.6 m/Speckle	2008 Jan 10			550 nm/30 nm	10 ms	10000/6000	36 Ori
BTA 6 m/Speckle	2008 Jan 26			550 nm/20 nm	20 ms	1500/2000	θ^1 Ori D
VLTI/AMBER	2007 Jan 08	04:36, 06:32	UT1-UT3-UT4	LR-K	26 ms	12000/10000	HD 41547
VLTI/AMBER	2007 Dec 03	07:19	A0-D0-H0	LR-HK	26 ms	5000/10000	HD 33833
VLTI/AMBER	2007 Dec 03	07:34, 08:44	A0-D0-H0	LR-HK	50 ms	7500/7500	HD 33833
VLTI/AMBER	2007 Dec 03	07:48, 08:54	A0-D0-H0	LR-HK	100 ms	2000/750	HD 33833
VLTI/AMBER	2007 Dec 05	06:05	A0-K0-G1	LR-HK	26 ms	5000/5000	HD 33833
VLTI/AMBER	2007 Dec 05	05:49, 07:28	A0-K0-G1	LR-HK	50 ms	10000/15000	HD 33833
VLTI/AMBER	2007 Dec 05	06:17, 07:46	A0-K0-G1	LR-HK	100 ms	3500/2500	HD 33833
VLTI/AMBER	2008 Feb 22	03:44	A0-D0-H0	LR-HK	50 ms	5000/10000	HD 37128, HD 50281
VLTI/AMBER	2008 Feb 22	04:21	A0-D0-H0	LR-HK	100 ms	2500/3500	HD 37128, HD 50281
VLTI/AMBER	2008 Feb 24	03:11	A0-K0-G1	LR-HK	50 ms	10000/5000	HD 37128
VLTI/AMBER	2008 Feb 24	02:37	A0-K0-G1	LR-HK	100 ms	6000/4000	HD 37128
VLTI/AMBER	2008 Mar 03	02:31	D0-H0-G1	LR-HK	50 ms	5000/5000	HD 43023
VLTI/AMBER	2008 Mar 03	02:52	D0-H0-G1	LR-HK	100 ms	1500/1500	HD 43023

method (Labeyrie 1970). For image reconstruction we used the bispectrum speckle interferometry method (Weigelt 1977, Weigelt & Wirnitzer 1983, Lohmann et al. 1983, Hofmann & Weigelt 1986).

Besides providing an independent astrometric measurement, our bispectrum speckle interferometric measurement is of special importance as it allows us to solve the 180°-ambiguity, which is inherent to long-baseline interferometric investigations which do not include the closure phase (e.g. Patience et al. 2008) or for which the instrumental closure phase sign has not yet been calibrated (as for VLTI/AMBER). Solving this ambiguity is essential for deriving the orbit of the system. Therefore, we paid special attention while deriving the field orientation of our speckle images, using calibration measurements which were taken with the same instrument setup during the same night as the θ^1 Ori C observations on θ^1 Ori A, θ^1 Ori B and the well-studied multi-component object η Carinae. For the January 2008 observations, a position angle calibration with an accuracy of $\sim 0.3°$ was done using K'-band observations covering the Trapezium stars θ^1 Ori A, B, and E, followed by the V' and B' observations of θ^1 Ori B, which is a binary system with a separation of $\sim 1''$, where the fainter component is a close binary with a separtion of $\sim 0''.15$. This allows us to unambiguously determine that in January 2008, the fainter component (C2) was located to the southwest of the primary star (Fig. 1 and A.1). Performing a detailed re-analysis on all Speckle data taken by our group between 1997 and 2005, we found a 180°-calibration problem which affected the position angle of the Speckle measurements at epochs 2003.8, 2003.9254, 2003.928, and 2004.8216, as published in Kraus et al. 2007. Since these Speckle measurements were used for the calibration of the IOTA and NPOI long-baseline interferometric observations by Kraus et al. (2007) and Patience et al. (2008), a revision of the preliminary orbital solutions presented in these papers is required (as presented in Sect. 5.1). In Tab. 3,
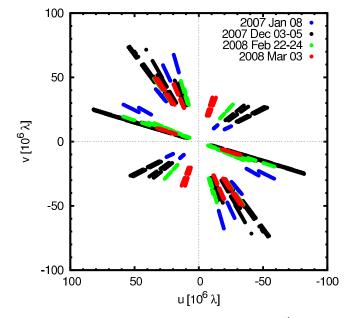

Fig. 2. uv-plane coverage obtained at four epochs on θ^1 Ori C with VLTI/AMBER. The radial extension of the uv-tracks reflects the spectral coverage of our AMBER interferometric data, covering either the K-band (LR-K mode, 2007 Jan 08) or the H- and K-band (LR-HK mode, 2007 Dec 03-05, 2008 Feb 22-24, 2008 Mar 03).

we list all available astrometric data, taking the quadrant correction into account.

2.2. VLTI/AMBER spectro-interferometry

AMBER is the NIR interferometric beam-combiner instrument (Petrov et al. 2007) of the Very Large Telescope Interferometer (VLTI), which is located on Cerro Paranal/Chile and operated by ESO. For the beam combination, either three 8.2 m unit telescopes (UTs) or three of the allocatable 1.8 m auxiliary tele-
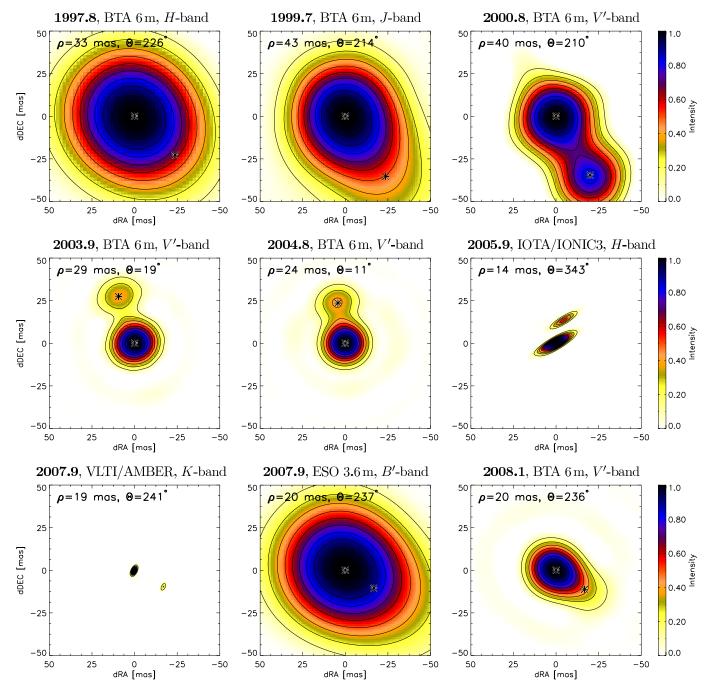
Fig. 1. Selection of interferometric images of the θ^1 Ori C system obtained by our group between 1997 and 2008, revealing the orbital motion of the companion. The images were reconstructed either from H-, J-, V'-, or B'-band speckle interferograms recorded at the BTA 6 m or the ESO 3.6 m telescopes, or from H-band Michelson interferograms recorded with the IOTA 3-telescope interferometer (see Kraus et al. 2007 for details). For epoch 2007.9, we show the aperture synthesis image which we reconstructed from VLTI/AMBER data using the procedure described in Sect. 4. For each image, 10% intensity level contours are shown. In the speckle images, the fitted component positions are marked with an asterisk.

scopes (ATs) can be used. One outstanding feature of AMBER is its spectral capability, allowing one to observe several spectral bands with low spectral resolution simultaneously (LR-JHK mode, $R = \lambda/\Delta\lambda = 35$, covering the J-band around 1.2 μm, the H-band around 1.6 μm, and the K-band around 2.2 μm). The wide wavelength coverage offered by this spectral mode allows us to fit the binary separation vector with a high accuracy and observing efficiency (as discussed in Sect. 3).

The VLTI/AMBER data was recorded in the course of three ESO programmes, yielding the uv-plane coverage shown in Fig. 2. For each science observation, we also recorded interferograms for at least one interferometric calibrator star (see Tab. 2 for the characteristics of our calibrator stars), which allows us to calibrate the visibilities and the closure phases for instrumental as well as atmospheric effects.

For AMBER data reduction, we employed the *amdlib2*-data reduction software [2] (release 2.1), which is based on the P2VM algorithm (Tatulli et al. 2007). For the LR-*HK* data, we applied the data selection criteria outlined in Kraus et al. (2008) in order to remove frames which were either degraded by atmospheric effects or were recorded significantly offset from zero optical path delay.

For the accuracy achievable with our binary model fits, the absolute calibration of the wavelength scale is of special importance. Therefore, we carefully refined the wavelength calibration using the telluric gaps between the observed spectral bands. Using this procedure (which is described in Appendix A), we reach a calibration accuracy of about 0.03 μm, which is still the dominating limiting factor on the total achievable astrometric accuracy ($\sim 2\%$).

While the target/calibrator observations from January 2007 were taken under good and stable atmospheric conditions, some of the observations in December 2007 and February 2008 suffer from strongly variable seeing conditions and short atmospheric coherence times. It is known that short coherence times can result in a decrease of the measured fringe contrast, which might not be completely calibrated out using calibrator measurements. This effect can impose errors on the absolute calibration, which are expected to increase with longer DIT and towards shorter wavelengths. To illustrate this effect, in Fig. 4 we plot the calibrated visibilities measured during our December 2007 observation campaign and compare them to the cosine visibility modulation of a binary source. In particular, in the *H*-band the resulting calibration errors can be on the order of 20%.

However, since all spectral channels of an AMBER interferogram are recorded at the same time, the wavelength-differential observables (in particular, the differential visibility $\delta V(\lambda)$) are practically insensitive to this degradation. Therefore, in Sect. 3 we employ a fitting algorithm in which we fit only differential visibilities and closure phases in order to determine the θ^1 Ori C binary separation vector.

A fundamental problem one encounters when interpreting VLTI/AMBER 3-telescope data concerns the lack of a calibration measurement for the closure phase sign, resulting in a 180° uncertainty on the position angle of binary star observations. Since our θ^1 Ori C VLTI/AMBER observations from December 2007 and February 2008 bracket the bispectrum speckle measurement from January 2008, our data set allows us to unambiguously define the closure phase sign for these observations, providing a direct calibration of the 180° uncertainty for VLTI/AMBER for the first time.

3. Modeling

In order to derive the binary separation ρ and position angle [3] Θ from the speckle data, we used the same algorithm as in our earlier studies on this system (Weigelt et al. 1999; Schertl et al.
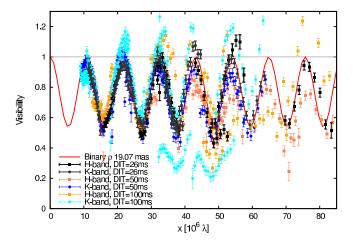
Fig. 4. AMBER visibilities measured on 2007 Dec 03 and 2007 Dec 05 plotted versus projected distance in the *uv*-plane (where the projection was perpendicular to the fitted binary separation vector $\Theta = 241.2°$, i.e. $x = u \cos(\Theta + 90°) - v \sin(\Theta + 90°)$). The solid red line shows the theoretical cosine visibility profile for a binary star with separation 19.07 mas and intensity ratio 0.30. As indicated by the strong visibility offsets, which particularly occur at high spatial frequencies, the absolute calibration is sometimes rather poor, reflecting the changing atmospheric conditions during these nights. It can also be seen that this calibration bias is particularly important for long DITs (50 ms, 100 ms), while it is nearly negligible for short DITs (26 ms, grey & black points). As expected, the spectral dependence of the visibility is not affected by these calibration uncertainties.

2003; Kraus et al. 2007), fitting a cosine function directly to the 2-D speckle visibilities. For illustration, in the Appendix (Fig. A.1) we show power spectra and Fourier spectra determined from three independent data sets obtained during our observing run with the ESO 3.6 m telescope and compare them with the model power and Fourier spectra corresponding to a binary star.

For the modeling of the AMBER data, we employed an optimized algorithm which fits closure phases (CP) and differential visibilities δV. Each AMBER LR-*HK* measurement records 16 *K*-band plus 11 *H*-band spectral channels in the wavelength range from 1.51 to 2.55 μm, covering about 40% of the object Fourier spectrum in radial direction (see *uv*-plane tracks in Fig. 2). Strongly resolved objects (such as binaries with a separation of $\rho \gtrsim \Delta\lambda/B$, where $\Delta\lambda$ is the recorded spectral window and B' is the projected baseline length) can already show significant visibility modulation over this range of spatial frequencies (see illustration in Fig. 3). For instance, our θ^1 Ori C AMBER measurements from December 2007 probe spatial frequencies out to the eighth lobe of the cosine binary visibility modulation (Fig. 4) and the wavelength-differential visibilities recorded in a single AMBER *H*-/*K*-band measurement sample up to 3 visibility cycles. This wavelength-differential visibility modulation already provides all information required to determine the binary separation and orientation. In this way, the absolute calibration of the visibility, which is subject to many adverse atmospheric effects, becomes dispensable.

To determine the differential visibilities δV as used in our fitting algorithm, we first follow the standard data reduction and calibration procedure in order to correct for wavelength-
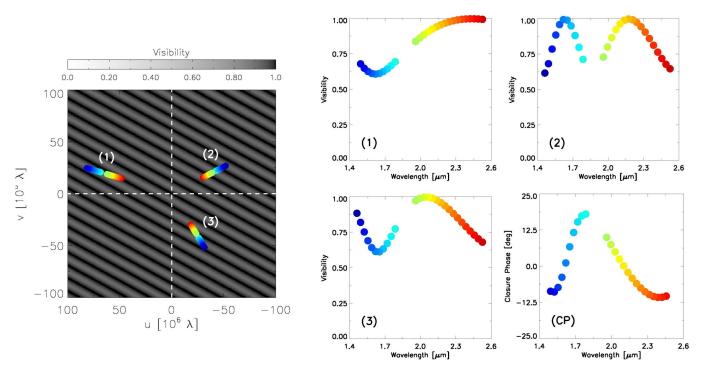
Fig. 3. Illustration of the basic principle of fitting binary parameters using wavelength-differential interferometric observables. *Left:* The VLTI/AMBER 3-telescope interferometer measures the interferometric observables in various spectral channels from 1.4 to 2.4 μm (as indicated by the color of the dots) and towards three different position angles, probing different regions in the two-dimensional Fourier spectrum of the source brightness distribution. The figure shows the visibility spectrum for a binary with $\rho = 19.07$ mas and $\Theta = 241.2°$ (as inferred for θ^1 Ori C on 2007 Dec 03) and the *uv*-sampling obtained with one of our AMBER observations on the same date. *Middle and Right:* The visibilities and phases show a wavelength-differential modulation which is independent of the absolute calibration (see Sect. 3) and which can be fitted to analytical models.

dependent instrumental effects (using a calibrator measurement taken during the same night). Then, we remove the absolute calibration by subtracting the average visibility of the considered spectral window

$$\delta V(\lambda) = V(\lambda) - \langle V(\lambda) \rangle_{\text{band}}, \tag{1}$$

yielding the differential visibility δV, which we compute separately for each spectral band (*H* and *K*-band).

A similar approach is applied to the model visibilities $V_{\text{model}}(\lambda)$ (which we compute using equations 7, 11, and 12 from Kraus et al. 2005):

$$\delta V_{\text{model}}(\lambda) = a \left(V_{\text{model}}(\lambda) - b \right), \tag{2}$$

where a and b are adjusted to minimize the residuals between the model visibilities and the measured wavelength-differential visibilities $\delta V(\lambda)$ before a Levenberg-Marquardt least-square fitting algorithm is used to determine the best-fit model parameters. The measured closure phases are fit simultaneously with the differential visibilities, weighting each data point according to the determined error bars (see equations 8–10 in Kraus et al. 2005). Parameters in our binary star model are the binary separation ρ, the position angle Θ, the intensity ratio F_{C2}/F_{C1}, and the uniform disk diameter of the components. Since our earlier speckle measurements indicated that F_{C2}/F_{C1} is practically constant in the NIR wavelength range (see Kraus et al. 2007), we assume that the intensity ratio does not vary over the *H*- and *K*-bands. For the model fitting, we fix the apparent

diameters of the two stars to 0.22 mas for the primary star (corresponding to 10.6 $R_\odot$ at a distance of 450 pc) and 0.15 mas for the companion (7.2 $R_\odot$, using the spectral type determined by Kraus et al. 2007 and the stellar evolutionary models of Martins et al. 2005). Our AMBER LR measurements and best-fit models are shown in Fig. 5 and 6. The derived astrometric data are given in Tab. 3.

4. VLTI/AMBER aperture synthesis imaging

Currently, the most commonly applied procedure to extract scientific information from optical interferometric data is model fitting, which requires the selection of an appropriate (geometrical or astrophysically motivated) model, whose parameters are then adjusted to fit the interferometric observables. Since this model fitting approach requires *a priori* knowledge about the source structure, it might, in some cases, not be applicable or might lead to biased results. Therefore, it is highly desirable that optical interferometers such as VLTI/AMBER have the capability of recovering the source brightness distribution free of any assumptions. The aim of this section is to apply state-of-the-art aperture synthesis imaging techniques for the first time to real VLTI/AMBER data in order to independently confirm the scientific results obtained for θ^1 Ori C in the last section, and, simultaneously, to demonstrate the imaging capabilities of VLTI/AMBER on a relatively well-studied astrophysical target with limited intrinsic complexity.
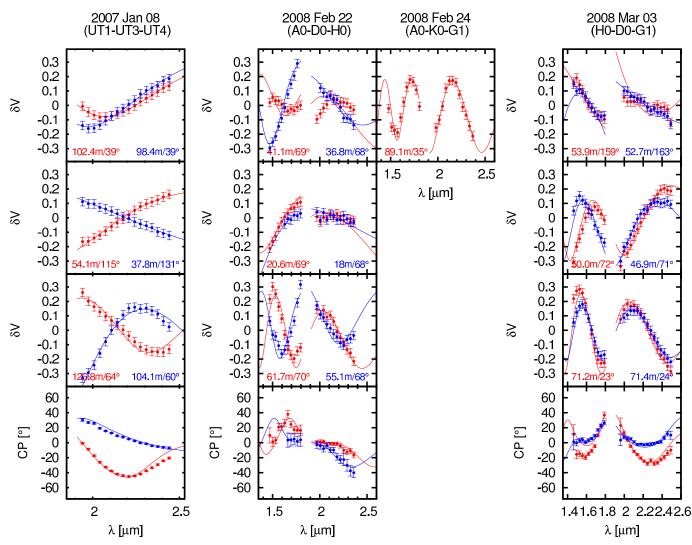
Fig. 5. Differential visibilities and closure phases measured with VLTI/AMBER in January 2007 *(left)*, February 2008 *(middle)*, and March 2008 *(right)* on θ^1 Ori C. The solid lines show the best-fit model corresponding to the binary parameters given in Tab. 3.

In order to obtain the *uv*-coverage required for aperture synthesis imaging, we combined the θ^1 Ori C AMBER data sets taken between December 2007 and March 2008 on three different 3-telescope array configurations and at several hour angles. Assuming that the source morphology does not change significantly over the *K*-band (which seems well justified based on our earlier measurements of the wavelength-dependent binary flux ratio; Kraus et al. 2007), we make use of AMBER's spectral coverage, yielding radial tracks in the *uv*-plane (Fig. 7, *left*). Since the *K*-band visibilities provide a more reliable absolute calibration (see Sect. 2.2), we did not use the *H*-band data for image reconstruction and rejected also one measurement taken under particularly poor and variable conditions (2007 Dec 05, UT 07:46). In order to correct for the binary orbital motion over the 3-month period ($\Delta\rho = 2.2$ mas, $\Delta\Theta = 6.6°$), we apply a rotation-compensating coordinate transformation of the *uv*-plane (see Kraus et al. 2005 for a description of this procedure) using the astrometric data given in Tab. 3. Then, we employed our *Building Block Mapping* software, which is based on the algorithm described by Hofmann & Weigelt (1993). Starting from an initial single δ-function, this algo-

rithm adds components to a model image in order to minimize the deviations between the measured bispectrum and the bispectrum of the model image. Finally, the image is convolved with a clean beam of $\sim 1.5 \times 3$ mas, reflecting the elongation of the sampled *uv*-plane. The resulting *K*-band aperture synthesis image (Fig. 1 and Fig. 7, *right*) yields a direct, model-independent representation of our VLTI/AMBER interferometric data. Measuring the companion position in the reconstructed image ($\rho = 19.3$ mas, $\Theta = 241°$, epoch 2007.9), we find good agreement with the results obtained with our model fitting approach using wavelength-differential observables (Sect. 3). The noise features within the image show an intensity amplitude below 2% of the peak brightness in the image.

5. Results

5.1. Dynamical orbit of the θ^1 Ori C binary system

Since our new astrometric data extend the orbital coverage for the θ^1 Ori C system by about 12 months and solves the calibra-
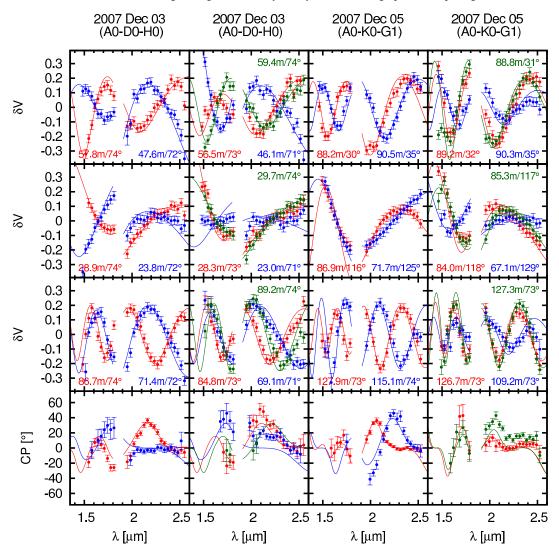
Fig. 6. Similar to Fig. 5, showing the AMBER data and best-fit model for our observations from December 2007

.

tion problem described in Sect. 2.1, we can significantly improve the orbital solution of the system. To derive a refined orbital solution, we applied two independent orbit fitting approaches.

First, we used the method presented by Docobo (1985), which generates a family of Keplerian orbits, whose apparent orbits pass through three base points. These base points might be selected from the actual astrometric measurements or represent observationally favored areas in the (ρ, Θ, t) parameter space. From the generated class of possible solutions, the orbit which best agrees with the measured separations and PAs is selected. We use the error bars of the individual measurements as weight. The orbital elements for the determined best-fit orbit solution are given in Tab. 4.

In addition, we implemented a grid search algorithm which scans the parameter space of the dynamical elements eccentricity e, period P, and time of periastron passage T_0. As described by Hilditch (2001), at each grid point, the geometrical orbital elements a, i, Ω, and ω can be determined by fitting the Thiele-Innes constants to the observational data. We scanned the parameter space between $P = 9 \ldots 16$ yrs (in in-

crements of 0.001 yrs), $e = 0.0 \ldots 1.0$ (in increments of 0.005), and $T_0 = 2000.0 \ldots 2010.0$ (in increments of 0.001 yrs) and determined the least-square distance between the N measured positions (ρ_i, Θ_i) and the corresponding orbit positions (ρ'_i, Θ'_i) for each orbit solution:

$$\chi_r^2 = \frac{1}{N} \sum_{i=1\ldots N} \left[\left(\frac{\rho_i - \rho'_i}{\sigma_{\rho_i}} \right)^2 + \left(\frac{\Theta_i - \Theta'_i}{\sigma_{\Theta_i}} \right)^2 \right] \qquad (3)$$

Using the χ_r^2 value determined at each grid point, we built a $\chi_r^2(P, e, T_0)$ data cube, which we projected to determine the local minimum and the associated uncertainty for each parameter. Fig. 9 shows the determined χ_r^2 minima curves, from which we determine the best-fit orbital elements given in Tab. 4. Given that the orbital coverage has been substantially improved since our 2007 study, we do not have to impose *a priori* constraints on the distance/system mass in order to eliminate unphysical orbit solutions. In Fig. 8c we compare the orbital solutions determined with the Docobo (1985) algorithm and with the grid search algorithm to the available astrometric data.

Table 3. Astrometric measurements for the θ^1 Ori C binary system.

Telescope	Date	Filter	Flux ratio F_{C2}/F_{C1}	Θ [°]	ρ [mas]	Ref.
BTA 6 m/Speckle	1997.784	H	0.26 ± 0.02	226.0 ± 3	33 ± 2	a
BTA 6 m/Speckle	1998.838	K'	0.32 ± 0.03	222.0 ± 5	37 ± 4	a
BTA 6 m/Speckle	1999.737	J	0.31 ± 0.02	214.0 ± 2	43 ± 1	b
BTA 6 m/Speckle	1999.8189	G'	0.35 ± 0.04	213.5 ± 2	42 ± 1	c
BTA 6 m/Speckle	2000.8734	V'	0.35 ± 0.03	210.0 ± 2	40 ± 1	c
BTA 6 m/Speckle	2001.184	J	0.29 ± 0.02	208.0 ± 2	38 ± 1	b
BTA 6 m/Speckle	2003.8	J	0.30 ± 0.02	19.3 ± 2	29 ± 2	c
BTA 6 m/Speckle	2003.9254	V'	–	19.0 ± 2	29 ± 2	c
BTA 6 m/Speckle	2003.928	V'	–	19.1 ± 2	29 ± 2	c
BTA 6 m/Speckle	2004.8216	V'	0.34 ± 0.04	10.5 ± 4	24 ± 4	c
IOTA	2005.92055	H	0.28 ± 0.03	342.74 ± 2	13.55 ± 0.5	c
NPOI	2006.1486	V	–	332.3 ± 3.5	11.80 ± 1.11	d
VLTI/AMBER	2007.0192	K	0.31 ± 0.03	274.9 ± 1	11.04 ± 0.5	–
NPOI	2007.1425	V	–	268.1 ± 5.2	11.94 ± 0.31	d
NPOI	2007.1507	V	–	272.9 ± 8.8	12.13 ± 1.58	d
NPOI	2007.1753	V	–	266.6 ± 2.1	12.17 ± 0.37	d
NPOI	2007.2055	V	–	265.6 ± 1.9	12.28 ± 0.41	d
NPOI	2007.2137	V	–	263.0 ± 2.3	12.14 ± 0.43	d
BTA 6 m/Speckle	2007.9014	V'	0.29 ± 0.02	238.0 ± 2	19.8 ± 2	–
VLTI/AMBER	2007.9233	$H+K$	0.24 ± 0.07	241.2 ± 1	19.07 ± 0.5	–
ESO 3.6 m/Speckle	2008.0274	B'	0.29 ± 0.02	237.0 ± 3	19.7 ± 3	–
ESO 3.6 m/Speckle	2008.0274	V'	0.31 ± 0.02	236.5 ± 3	19.6 ± 3	–
BTA 6 m/Speckle	2008.0712	V'	0.31 ± 0.02	236.2 ± 2	20.1 ± 2	–
VLTI/AMBER	2008.1479	$H+K$	0.23 ± 0.09	234.6 ± 1	21.17 ± 0.5	–
VLTI/AMBER	2008.1726	$H+K$	0.26 ± 0.06	236.4 ± 1	21.27 ± 0.5	–

Notes – The position angles given in col. 5 are measured East of North and were corrected for the 180°-calibration problem described in Sect. 2.1.

References – (*a*) Weigelt et al. 1999, (*b*) Schertl et al. 2003, (*c*) Kraus et al. 2007, (*d*) Patience et al. 2008.

5.2. Constraining the binary mass ratio

Besides the 15.424-day period which is associated with the wind from the primary, long-term radial velocity variations were also found (Vitrichenko 2002; Stahl et al. 2008). Using a large data set covering more than 15 yrs of spectroscopic observations (plus three archival measurements, which extend the coverage to more than 64 yrs), Stahl et al. (2008) showed that these variations are consistent with the orbital motion of a high-eccentricity binary system. Although the strong scatter within the radial velocity measurements prevents us from solving for the precise spectroscopic orbit, the combination of these data with our new orbital solution can be used to provide a first direct constraint on the mass ratio of the components in the θ^1 Ori C system.

In Fig. 10 we plot the available radial velocity data as a function of orbital phase using the orbital period P and time for periastron passage T_0 determined independently from our interferometric measurements (Sect. 5.1). Using the method from Pourbaix (1998), we compute the radial velocity variations corresponding to our full set of orbital elements (Tab. 4) and perform a least-square fit between the measured (v_i) and the predicted (v'_i) radial velocities in order to determine the mass-ratio between the binary components. As least-square measure for N measurements, we use

$$\chi_r^2 = \frac{1}{N} \sum_{i=1...N} \left(\frac{v_i - v'_i - V_0}{\sigma_{v_i}} \right)^2, \qquad (4)$$

where V_0 is the velocity of the center of mass of the system, which is given by $V_0 := \langle v_i \rangle - \langle v'_i \rangle$. Since the radial velocities were extracted from various spectral lines (C IV, He II, and O III) and it is known that these lines can show, with respect to each other, systematic velocity offsets on the order of $2 - 3$ km s^{-1} (Stahl et al. 2008), we used 3 km s^{-1} as minimum velocity error σ_{v_i} in order to avoid overweighting individual measurements. By varying the mass-ratio between the components, we find

$$q(d) := \frac{M_{C1}}{M_{C2}} = \left(5.27^{+1.17}_{-0.75} \frac{d}{414 \text{ pc}} - 1 \right)^{-1}, \qquad (5)$$

i.e. $q(450 \text{ pc}) = 0.21 \pm 0.04$ or $q(414 \text{ pc}) = 0.23 \pm 0.05$, which is slightly lower than the value we derived earlier by modeling the wavelength-dependent binary flux ratio of the θ^1 Ori C system ($q = 0.45 \pm 0.15$, Kraus et al. 2007).

For the radial velocity of the center of mass, we determine 23.6 km s^{-1}, which is in good agreement with the heliocentric velocity of the Orion Molecular Cloud (~ 28 km s^{-1}, O'Dell 2001). This might indicate that the relative motion of
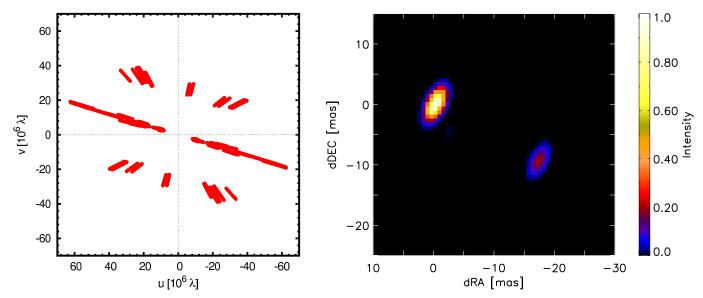
Fig. 7. Combining AMBER data obtained on three telescope configurations (*Left: uv*-coverage), we reconstructed an aperture synthesis image of the θ^1 Ori C system with an effective resolution of ~ 2 mas (*Right*). For a detailed description, we refer to Sect. 4.
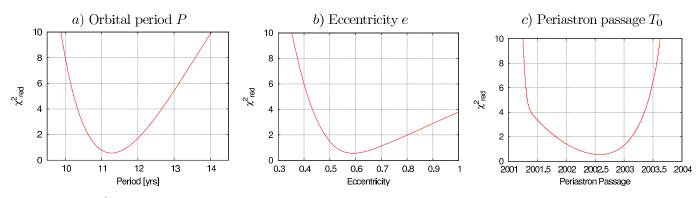

Fig. 9. Minimum χ^2_r curves as function of the dynamical orbital parameters P, e, T_0. These curves were used to determine the best-fit orbit solution and to evaluate the uncertainties on the individual parameters (see Tab. 4).

the θ^1 Ori C system with respect to the parental cloud is smaller than previously assumed (O'Dell 2001; Stahl et al. 2008).

5.3. Dynamical masses and parallaxes

Kepler's third law ($M_{\text{system}} \cdot \pi^3 = a^3/P^2$) relates a and P with the product of the system mass $M_{\text{system}} := M_{\text{C1}} + M_{\text{C2}}$ and the cube of the parallax π. Therefore, our astrometric measurement of a^3/P^2 directly constrains certain areas in the (π, M_{system}) parameter space, as shown by the shaded area in Fig. 13. Since the elements of the spectroscopic orbit are currently only weakly constrained, it is not possible to directly separate the system mass and the dynamical parallax. However, several independent methods exist to disentangle these important parameters using additional information, such as the flux ratio of the components, their mass ratio, and/or their stellar parameters.

The stellar parameters of θ^1 Ori C1 have already been studied extensively with spectroscopy, placing the effective temperature between 37 000 and 40 000 K (e.g. Rubin et al. 1991; Baldwin et al. 1991; Simón-Díaz et al. 2006; Polyakov & Tsivilev 2007). In particular, Simón-Díaz et al. (2006) included non-LTE and line-blanketing effects ($T_{\text{eff,C1}} = 39\,000 \pm 1000$ K)

for their detailed spectroscopic modeling, which makes their results compatible with the O-star stellar parameter calibration by Martins et al. (2005).

Since each of the above-mentioned stellar or observational parameters is associated with certain assumptions and uncertainties, it seems advisable to take a number of alternative approaches for deriving the underlying physical parameters in order to yield some insight into the associated uncertainties. Therefore, we follow three alternative approaches:

a) Based on the effective temperature determination of the primary and the binary flux ratio, one can give a reasonable mass range for each component and, thus, the system mass (green-shaded area in Fig. 13).

b) One can estimate the mass of the primary from the stellar temperature and then derive the companion mass using the mass ratio constraints obtained from the radial velocities (Sect. 5.2), yielding the orange curve in Fig. 13.

c) Baize & Romani (1946) presented a method which solves for the system mass and the dynamical parallax using a mass-luminosity relation (MLR), the bolometric corrections of the components and their extinction-corrected apparent magnitudes. To evaluate the influence of the MLRs
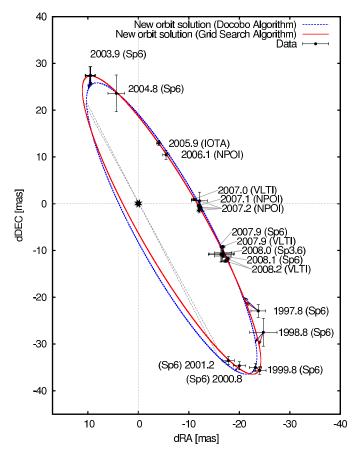
Fig. 8. Comparison of our new orbit solutions with the available astrometric data. Each position measurement is connected to the orbit prediction with an *O–C* vector (arrows). Furthermore, we show the lines of nodes in grey. The plots are centered on the primary star. North is up and east is to the left.
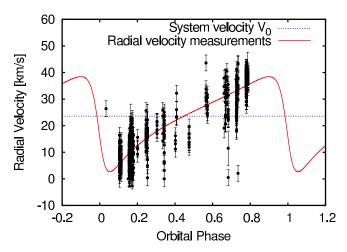

Fig. 10. The radial velocities measured towards θ^1 Ori C plotted as function of orbital phase (assuming the orbital elements determined with our grid search algorithm; see Tab. 4). Besides the extensive data set by Stahl et al. (2008), we included the radial velocities measured by Struve & Titus (1944), Conti (1972), and Morrell & Levato (1991). The red line shows the radial velocities corresponding to our orbital solution with a system velocity $V_0 = 23.6$ km s^{-1} (blue dashed line) and the mass ratio $q(414$ pc$) = 0.23$ as determined from our least-square fit (Sect. 5.2).

Table 4. Orbital elements as determined with the algorithm from Docobo (1985) and our grid search algorithm (described in Sect. 5.1).

Parameter		Docobo algorithm	Grid search algorithm
P	[yrs]	11.05 ± 0.03	11.26 ± 0.5
T_0		2002.87 ± 0.40	2002.57 ± 0.5
e		0.534 ± 0.050	0.592 ± 0.07
a	[mas]	40.00 ± 3.00	43.61 ± 3
i	[°]	100.7 ± 1.0	99.0 ± 2.6
Ω	[°]	25.3 ± 1.5	26.5 ± 1.7
ω	[°]	290.9 ± 2.5	285.8 ± 8.5
χ_r^2		1.84	0.56
a^3/P^2	[mas^3/yrs^2]	524 ± 130	645 ± 200
M_{C1}/M_{C2}		0.21 ± 0.05	0.23 ± 0.05
$M_{C1} + M_{C2}$	[$M_\odot$]	49 ± 4	47 ± 4
d_{dyn}	[pc]	456 ± 13	416 ± 12

Notes – Besides the orbital elements, we give the mass ratio (Sect. 5.2), dynamical distance, and system mass (Sect. 5.3), derived from both set of orbit elements. The dynamical distance and system mass was determined using the method from Baize & Romani (1946, method *c* in Sect. 5.3) and three different MLRs. When assuming another distance d', the dynamical system mass $M_{C1} + M_{C2}$ must be scaled by a factor $(d'/d_{dyn})^3$. The mass ratio M_{C1}/M_{C2} was also computed for the distance d_{dyn}, but can be converted to any other distance using equation 5.
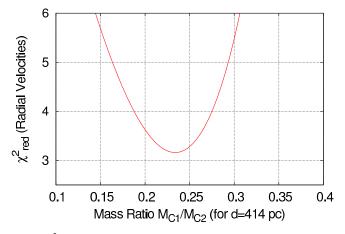

Fig. 11. χ_r^2 curve for our fit of the binary mass ratio to the available radial velocity data (assuming a distance of 414 pc). We assume the orbital elements (Tab. 4) derived from our interferometric measurements.

on the result, we used three different MLRs; namely, from Baize & Romani (1946), Heintz (1978), and Demircan & Kahraman (1991) (corresponding to the three blue data points in Fig. 13).

For methods *a)* and *b)*, we employ the stellar calibration by Martins et al. (2005), while for method *c)*, three earlier calibrations are used. In method *a)* and *b)*, the stellar temperature of the primary component is fixed to the value by Simón-Díaz et al. (2006, $T_{eff,C1} = 39\,000 \pm 1000$ K), while in *c)* we scan a slightly wider range of temperature values ($T_{eff,C1} = 37\,000 \ldots 40\,000$ K, $T_{eff,C2} = 30\,000 \ldots 33\,000$ K, using the bolometric correction by Bessell et al. 1998). Method *a)* requires the V'-band flux ratio ($F_{C2}/F_{C1} = 0.31 \pm 0.02$)
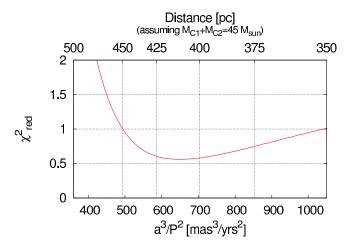
Fig. 12. Minimum χ^2_r curve as a function of $a^3/P^2 = (M_{\mathrm{system}}) \cdot \pi^3$, through which the dynamical orbital parameters can be related to the mass sum and the dynamical parallax. For illustration, we give the dynamical distance in the upper axis assuming a total system mass of $45\,M_\odot$.
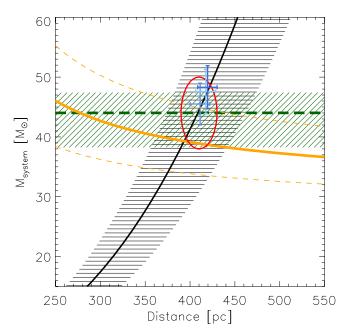

Fig. 13. The derived a^3/P^2 value puts some direct constraints on the system mass $M_{\mathrm{system}} := M_{\mathrm{C1}} + M_{\mathrm{C2}}$ and the dynamical distance. As described in Sect. 5.3, we employ three alternative methods to obtain constraints, which help to disentangle the system mass and the distance (method *a:* dashed green-shaded area, method *b:* orange curve, method *c:* blue data points). The black-shaded area marks the a^3/P^2-constraints determined with our orbit grid search algorithm. With the red ellipse, we visually mark the area of best agreement between all constraints.

and *c)* the extinction-corrected magnitude of the total system ($V = 5.12 \pm 0.1$, $A_V = 1.74 \pm 0.1$, Hillenbrand 1997).

Evidently, each method is associated with considerable uncertainties, which makes it very desirable for future observations to improve not only the astrometric orbit, but to derive the accurate spectroscopic orbit of the system as well. Nevertheless, within their large uncertainties, the methods employed cover a common area in parameter space, corresponding

to a system mass of $M_{\mathrm{system}} = 44 \pm 7\,M_\odot$ and a dynamical distance of $d = 410 \pm 20$ pc, as marked with the red ellipse in Fig. 13. Methods *a)* and *b)* yield systematically lower system masses than method *c)*, reflecting the recent correction in the mass calibration scale in stellar evolutionary models (Martins et al. 2005). Assuming a distance of 414 pc, as determined by Menten et al. (2007), would yield a system mass of $46\,M_\odot$.

5.4. Possible implications on the dynamical history of the θ^1 Ori C system

With an eccentricity of ~ 0.6, the orbit of θ^1 Ori C is located on the upper end of the eccentricity distribution of low- as well as high-mass binary stars (Mathieu 1994; Mason et al. 1998), perhaps providing important information about the dynamical history of the system. Tan (2004, 2008) proposed that the Becklin-Neugebauer (BN) object, which is located 45″ northwest of the Trapezium stars, might be a runaway B star ejected from the θ^1 Ori C multiple system approximately 4 000 yrs ago. This scenario is based on proper motion measurements, which show that BN and θ^1 Ori C recoil roughly in opposite directions. Three-body interaction is a crucial part of this interpretation, and the high eccentricity of the θ^1 Ori C orbit which we derive for this system might be a direct consequence of this dynamical interaction event. However, another study (Rodríguez et al. 2005) also aimed to identify the multiple system from which BN was ejected and identified Source I as the likely progenitor system. Later, Gómez et al. (2005, 2008) added further evidence to this interpretation by identifying Source *n* as a potential third member of the decayed system. Therefore, it is still unclear whether this scenario can explain the measured properties of the θ^1 Ori C orbit.

As an alternative explanation for the high eccentricity of the θ^1 Ori C system, Zinnecker & Yorke (2007) pointed out that such systems are predicted by star formation scenarios which include sub-Keplerian rotating disks or filament fragmentation (Kratter & Matzner 2006).

6. Conclusions

We have presented new bispectrum speckle (V'-/B'-band) and VLTI/AMBER (H-/K-band) interferometric observations of the Orion Trapezium star θ^1 Ori C covering several epochs over a time period of about 14 months.

From our long-baseline interferometric data, we have reconstructed the first model-independent VLTI/AMBER aperture synthesis image, depicting the θ^1 Ori C system at a resolution of ~ 2 mas and demonstrating the imaging capabilities of this unique facility. In order to extract accurate astrometric information for all epochs, we have followed a new modeling approach which is based on wavelength-differential observables and which demonstrates the benefits of spectro-interferometry in terms of observing efficiency and robustness to poor observing conditions. Furthermore, our ESO 3.6 m and the BTA 6 m speckle observations allow us to solve 180°-ambiguity and to calibrate the closure phase sign of our VLTI/AMBER observations, providing a potential reference for other AMBER observations using closure phase information.
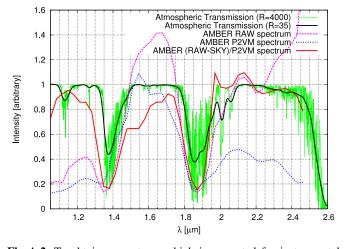
Fig. A.2. To obtain a spectrum which is corrected for instrumental effects for the spectral calibration, we subtract from the RAW spectrum the SKY spectrum and then divide by the P2VM spectrum (blue dashed curve). The resulting instrument-corrected spectrum (red curve) is compared with an atmospheric transmission spectrum (green curve: $R = 4000$; black curve: $R = 35$).

Our new θ^1 Ori C astrometric data shows that since its discovery in 1997, the θ^1 Ori C companion has nearly completed one orbital revolution and that the system has a high eccentricity ($e \sim 0.6$). Solving for the orbital elements, we determine a period of ~11.3 yrs, a semi-major axis of 44 mas, and a periastron passage around 2002.6. According to our orbital solutions, the physical separation between the components decreases to ~ 7 AU (2.8 mas) during periastron passage, which might be too large to result in detectable signatures of wind-wind interaction between the stellar winds.

Using additional information about the stellar parameters and various stellar models, we estimate the total system mass to be $44 \pm 7\, M_\odot$ and the dynamical distance to be $d = 410 \pm 20$ pc. In the coming years, the uncertainties on these parameters could be considerably reduced with new spectroscopic and astrometric observations of this important binary system.

Appendix A: Spectral calibration of AMBER-LR data

Employing wavelength-differential visibilities and phases for model fitting requires a precise knowledge of the central wavelength of the recorded spectral channels. Therefore, we performed a re-calibration of the wavelength axes of our data sets using atmospheric absorption features and found deviations of up to ~ 0.1 μm compared to the standard wavelength table applied to the data on Paranal.

In the recorded J-/H-/K-band object raw spectra, the telluric features are not pronounced enough to be used for the calibration, which is mainly due to absorption by internal optical components. Therefore, besides the raw spectrum of the

object exposures, we also extracted the spectrum from the sky and the P2VM calibration exposures. The P2VM calibration files (P2VM=*Pixel-to-Visibility-Matrix*; see Tatulli et al. 2007) are recorded at the beginning of each observation block using a lamp located in AMBER's *Calibration and Alignment Unit* and provide a measure of the instrumental transmission. By subtracting the sky spectrum from the object spectrum and then dividing by the P2VM spectrum, we yield a spectrum which is corrected for most instrumental effects and shows the telluric absorption features much more clearly (see Fig. A.2, red curve). These corrected spectra were compared with standard atmospheric transmission spectra provided by the Gemini observatory[4] (see Fig. A.2, green curve). We manually align the spectra using the pronounced gaps between the J-/H- and H-/K-band and find best agreement assuming a linear dispersion law $\lambda(i) \propto 0.0328 \cdot i$, where i is the number of the spectral channel on the detector.

The remaining wavelength calibration uncertainty of about 1 spectral channel (corresponding to about 0.03 μm) is the dominant limiting factor on the achievable astrometric accuracy (~ 2%). Therefore, for future observations, it seems highly desirable to implement an AMBER on-site spectral calibration device (e.g. NIR lasers with well-known frequencies), fascilitating an absolute spectral calibration in the standard instrument calibration procedure, pushing AMBER to its full astrometric accuracy.

References

Baize, P. & Romani, L. 1946, Annales d'Astrophysique, 9, 13
Baldwin, J. A., Ferland, G. J., Martin, P. G., et al. 1991, ApJ, 374, 580
Bessell, M. S., Castelli, F., & Plez, B. 1998, A&A, 333, 231
Conti, P. S. 1972, ApJ, 174, L79+
Demircan, O. & Kahraman, G. 1991, Ap&SS, 181, 313
Docobo, J. A. 1985, Celestial Mechanics, 36, 143
Genzel, R. & Stutzki, J. 1989, ARA&A, 27, 41
Gómez, L., Rodriguez, L. F., Loinard, L., et al. 2008, ArXiv e-prints, 805
Gómez, L., Rodríguez, L. F., Loinard, L., et al. 2005, ApJ, 635, 1166
Heintz, W. D. 1978, Geophysics and Astrophysics Monographs, 15
Herbig, G. H. & Terndrup, D. M. 1986, ApJ, 307, 609
Hilditch, R. W. 2001, An Introduction to Close Binary Stars (An Introduction to Close Binary Stars, by R. W. Hilditch, pp. 392. ISBN 0521241065. Cambridge, UK: Cambridge University Press, March 2001.)
Hillenbrand, L. A. 1997, AJ, 113, 1733
Hirota, T., Bushimata, T., Choi, Y. K., et al. 2007, PASJ, 59, 897
Hofmann, K.-H. & Weigelt, G. 1986, A&A, 167, L15+
Hofmann, K.-H. & Weigelt, G. 1993, A&A, 278, 328

---

[4] These ATRAN transmission spectra can be found on the website http://www.gemini.edu/sciops/telescopes-and-sites/observing-condition-constraints/transmission-spectra.
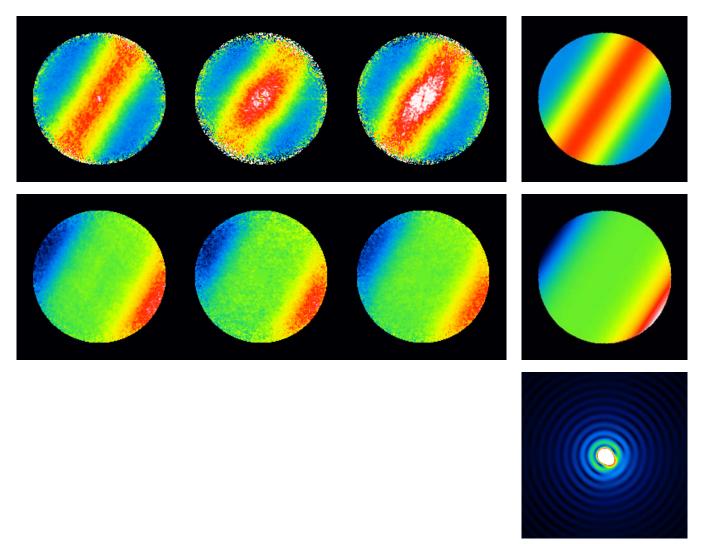
Fig. A.1. *Left:* Three two-dimensional average power spectra (*top row*) and Fourier phase spectra (*middle row*) derived from *B'*-band speckle data recorded on 2008 Jan 10 with the ESO 3.6 m telescope. *Right:* Comparing this data to model power spectra (*top row*) and Fourier spectra (*middle row*) for a binary with separation $\rho = 19.7$ mas and PA $\Theta = 237°$ shows that the fainter component is located southwest of the primary star (the bispectrum speckle image reconstructed from the model visibilities and phases are shown to the bottom right). Together with the calibration data sets mentioned in Sect. 2.1, this data set unambigously defines the current orientation of the θ^1 Ori C binary system and shows that the system has nearly completed one orbital revolution since its discovery in 1997.

Jeffries, R. D. 2007, MNRAS, 376, 1109

Kratter, K. M. & Matzner, C. D. 2006, MNRAS, 373, 1563

Kraus, S., Balega, Y. Y., Berger, J.-P., et al. 2007, A&A, 466, 649

Kraus, S., Preibisch, T., & Ohnaka, K. 2008, ApJ, 676, 490

Kraus, S., Schloerb, F. P., Traub, W. A., et al. 2005, AJ, 130, 246

Labeyrie, A. 1970, A&A, 6, 85

Lohmann, A. W., Weigelt, G., & Wirnitzer, B. 1983, Appl. Opt., 22, 4028

Martins, F., Schaerer, D., & Hillier, D. J. 2005, A&A, 436, 1049

Mason, B. D., Gies, D. R., Hartkopf, W. I., et al. 1998, AJ, 115, 821

Mathieu, R. D. 1994, ARA&A, 32, 465

Mayne, N. J. & Naylor, T. 2008, MNRAS, 326

McCaughrean, M. J. & Stauffer, J. R. 1994, AJ, 108, 1382

Menten, K. M., Reid, M. J., Forbrich, J., & Brunthaler, A. 2007, A&A, 474, 515

Morrell, N. & Levato, H. 1991, ApJS, 75, 965

Mozurkewich, D., Johnston, K. J., Simon, R. S., et al. 1991, AJ, 101, 2207

O'Dell, C. R. 2001, ARA&A, 39, 99

Patience, J., Zavala, R. T., Prato, L., et al. 2008, ApJ, 674, L97

Petrov, R. G., Malbet, F., Weigelt, G., et al. 2007, A&A, 464, 1

Polyakov, A. M. & Tsivilev, A. P. 2007, Astronomy Letters, 33, 34

Pourbaix, D. 1998, A&AS, 131, 377

Rodríguez, L. F., Poveda, A., Lizano, S., & Allen, C. 2005, ApJ, 627, L65

Rubin, R. H., Simpson, J. P., Haas, M. R., & Erickson, E. F. 1991, ApJ, 374, 564

Sandstrom, K. M., Peek, J. E. G., Bower, G. C., Bolatto, A. D., & Plambeck, R. L. 2007, ApJ, 667, 1161

Schertl, D., Balega, Y. Y., Preibisch, T., & Weigelt, G. 2003, A&A, 402, 267

Simón-Díaz, S., Herrero, A., Esteban, C., & Najarro, F. 2006, A&A, 448, 351

Stahl, O., Kaufer, A., Rivinius, T., et al. 1996, A&A, 312, 539

Stahl, O., Wade, G., Petit, V., Stober, B., & Schanne, L. 2008, A&A, 487, 323

Stassun, K. G., van den Berg, M., Feigelson, E., & Flaccomio, E. 2006, ApJ, 649, 914

Struve, O. & Titus, J. 1944, ApJ, 99, 84

Tan, J. C. 2004, ApJ, 607, L47

Tan, J. C. 2008, ArXiv e-prints, 807

Tatulli, E., Millour, F., Chelli, A., et al. 2007, A&A, 464, 29

Vacca, W. D., Garmany, C. D., & Shull, J. M. 1996, ApJ, 460, 914

Vitrichenko, É. A. 2002, Astronomy Letters, 28, 324

Weigelt, G., Balega, Y., Preibisch, T., et al. 1999, A&A, 347, L15

Weigelt, G. & Wirnitzer, B. 1983, Optics Letters, 8, 389

Weigelt, G. P. 1977, Optics Communications, 21, 55

Zinnecker, H. & Yorke, H. W. 2007, ARA&A, 45, 481

List of Objects